Bulk/Shell Formalism in a Mathematical Model Predicts the Superimposed Oscillations

Observed on Osteoblastic Calcium Responses.

Abstract

The presence of P2 receptors (P2Rs) on bone forming osteoblasts suggests that purinergic signaling plays an important role in skeletal mechano-transduction. P2Rs are activated by extracellular ATP, triggering a large array of heterogeneous calcium signature responses that each appears to have a functional significance in osteoblasts. Mathematical modeling of this system has previously illustrated the significance of these receptors in inducing such calcium responses, and shown that as [ATP] increases, a transition from transient to oscillatory to transient responses can be generated. However, the experimental recordings of these calcium responses have also revealed the presence of low amplitude, high frequency *superimposed oscillations* that were not previously elucidated. To further examine the underlying dynamics of this phenomenon, an existing mathematical model of this system is expanded by dividing the cell into two compartments representing the *shell* (within 80 nm of cellular membrane) and *bulk* (rest of the cell). The resulting model is simulated using MATLAB to study these fast oscillations. Further, a R script is written to perform a clustering analysis on the recorded calcium data to distinguish between those that exhibit the fast calcium oscillations from those that do not. Our results revealed that the shell compartment representing the microdomains of calcium channels are responsible for the high frequency, low amplitude *superimposed oscillations*, while the bulk compartment is responsible for the low frequency, high amplitude broad calcium dynamics. Our model maintained the [ATP]-induced transition from a transient to oscillatory to transient Ca^{2+} responses. The clustering analysis, on the other hand, showed that there are 21 clusters and that 13 of these exhibited the fast oscillations. The role of pumps and P2Rs in generating these variations remains to be determined. These findings thus illustrate how calcium microdomain activity can induce the superimposed oscillations in osteoblasts.

Introduction

The human skeleton has the ability to alter its morphology and metabolism in order to adapt to varying external forces exerted by its environment (Yavropoulou et al., 2016). Extracellular ATP is released from cells into the extracellular milieu due to various mechanical stimuli such as stress and hydrostatic pressure, where the ATP then initiates intracellular signaling through P2 receptors (P2Rs). The presence of P2Rs on bone forming osteoblasts suggests that purinergic signaling plays an important role in skeletal mechano-transduction. (Xing et al., 2016).

P2Rs are known to modulate intracellular calcium (Ca^{2+}) concentrations, as well as other monovalent cations such as sodium (Na^+) and potassium (K^+). Osteoblasts express at least seven different P2Rs (P2X2, P2X5, P2X7, P2Y1, P2Y2, P2Y4, P2Y6), where each alters intracellular Ca^{2+} via different mechanisms. P2XRs are ATP-gated and nonspecific cation channels that directly increases Ca^{2+} influx across the plasma membrane upon activation (Xing et al., 2016), whereas P2YRs are metabotropic G-protein coupled receptors that induce Ca^{2+} release from the endoplasmic reticulum (ER). Upon activation, P2YRs stimulate the Gq protein signaling pathway, leading to the production of inositol triphosphate (IP_3), and then the activation of IP3 receptors (IP3Rs) expressed on the membrane of the ER (Burnstock, 2018; Xing et al., 2016).

The most highly expressed P2Rs on osteoblasts are P2Y2R and P2X7R. While P2Y2Rs have a high affinity to extracellular ATP and may respond to low ATP concentration ([ATP]), P2X7Rs have a low affinity for extracellular ATP and only respond at high [ATP]. Together, their expression covers an [ATP] range of five orders of magnitude ($10^{-7}M$ to $10^{-2}M$) (Mikolajewicz, Smith, Komarova and Khadra, 2021; Xing et al., 2016).

Fluorescent Ca^{2+} imaging techniques was utilized to demonstrate that when osteoblasts are subjected to increasing extracellular [ATP], their intracellular Ca^{2+} response shifts between three modes of activity: transient with a semi-pronounced narrow peak, slow oscillatory response superimposed on decaying profile, transient with pronounced wide peak. Additionally, the data showed that at the plateau

component of the dose response curve, the peak amplitude of Ca^{2+} response exhibits two local dips at a moderate (10^{-4} M) and elevated (10^{-2} M) [ATP] (Mikolajewicz, Smith, Komarova and Khadra, 2021).

Mikolajewicz et al. (2021) created a mathematical model which established the sufficiency of the P2Y2 and P2X7 receptors in re-creating the ATP-mediated Ca^{2+} responses in osteoblasts. Mikolajewicz et al. (2021) modelled the P2Y2 receptors based on the two-dimensional Li-Renzel model, which successfully captured the transitions between transient to oscillatory to transient dynamics (Li-Renzel, 1994). The inclusion of a Markov Model for P2X7R dynamics (Khadra et al., 2013) was responsible for generating the two dips in the Ca^{2+} dose response. Further, the model also included considerations for IP_3 dynamics and for many cell surface and ER membrane receptors such as the sarcoendoplasmic reticulum calcium transport ATPase (SERCA) and plasma membrane Ca^{2+} ATPase (PMCA) (Mikolajewicz, Smith, Komarova and Khadra, 2021).

Interestingly, the time series of Ca^{2+} responses exhibited another feature not previously accounted for in mathematical models or in data analysis, namely, the high frequency, low amplitude oscillations superimposed on the low frequency, high amplitude oscillations. While this behavior is evident in a large portion of time series Ca^{2+} responses, some curves do not exhibit these superimposed oscillations. This highlights the large heterogeneity observed in Ca^{2+} responses (Mikolajewicz, Smith, Komarova and Khadra, 2021). In this study we seek to expand the mathematical model in Mikolajewicz et al. (2021) in order to explore which physiological mechanisms are at play in producing the high frequency, low amplitude oscillations (fast oscillations), which are superimposed on the lower frequency, higher amplitude ones (slow oscillations).

The aforementioned fast oscillations are hypothesized to be caused by the presence of Ca^{2+} microdomains near the plasma membrane of the cell, which are local small volume pockets of high Ca^{2+} concentration. Rather than viewing Ca^{2+} signalling as a "common pool" event where Ca^{2+} rises and falls uniformly, it can better be understood as the spatial averaging of these localized, short-lived Ca^{2+} microdomains that exist near the membrane (shell compartment of cell), that diffuse to the center of the

cell (bulk compartment of cell). Calcium transients exhibit a greater rising rate and briefer duration in the submembrane layer than in the bulk cytosol due to the presence of cell membrane receptors, which contributes to a time scale separation between the shell and the bulk compartments of the cell. Physiologically, Ca^{2+} transients immediately beneath the cell membrane (fast oscillations) are critically involved in processes such as EC coupling, hormone secretion, and neurotransmitter release, which are thought to be driven by calcium concentration 10 to 100 times higher than those measured in the bulk cytosol (Wang et al., 2004).

In this study, a bulk-shell formalism is introduced in the mathematical model of Ca^{2+} dynamics in osteoblasts in order to elucidate between the fast and slow oscillations (Mikolajewicz, Smith, Komarova and Khadra, 2021). By explaining these fast oscillations, a stronger and more accurate understanding of the production of Ca^{2+} signals can be developed, while also providing the opportunity to connect modelling predictions to real physiological data associated with these fast oscillations. To better understand the large heterogeneity of time series Ca^{2+} responses that were obtained from the Komarova lab, a clustering analysis is performed to group similar signals together. This allows for biophysical predictions about osteoblastic Ca^{2+} signalling to be made based on how the model's parameter regime varies based on the cluster it is reproducing. Finally, these biophysical predictions may be explored and confirmed experimentally in future studies.

Methods

Intracellular free [Ca^{2+}] recordings

Nicholas Mikolajewicz and Svetlana B Komarova, from the Faculty of Dentistry, McGill University, provided the experimental data. The procedure is identical to how it was described in (Mikolajewicz, Smith, Komarova and Khadra, 2021): In brief, C2-OB osteoblasts were loaded with Fura2-AM for 30 min, acclimatized in physiological solution for 10 min on the stage of an inverted fluorescence microscope, and imaged. To assess ATP dose-dependencies, the cells were bathed in 270 µL physiological solution and 30 µL ATP solution at 10x the final concentration.

Mathematical model

The physiological system of Ca^{2+} signalling in osteoblasts is modelled as a system of deterministic ordinary differential equations (ODEs). Fluxes contributing to an increase in the respective value of the dynamic variable are positive, while fluxes that decrease it are negative. The following discussion will motivate equations (2) to (11), which are described visually by Figure 1. The values of the parameters in the model are given in Table 1 in the appendix.

To develop a model for Ca^{2+} dynamics, the cell is divided into three compartments: the ER, the shell compartment of the cytosol (the region from the plasma membrane to 80 nm deep in the cell), and the bulk compartment of the cytosol (the remaining inner region of the cell). The respective Ca^{2+} concentrations in each of these compartments are denoted by $[Ca^{2+}]_{ER}$, $[Ca^{2+}]_S$, $[Ca^{2+}]_B$, and vary with time (according to Eqs. (8), (2), (5) respectively). To calculate cytosolic Ca^{2+} concentration ($[Ca]_{Cyt}$), the following formula is used

$$[Ca]_{Cyt} = \frac{V_S[Ca]_S + V_B[Ca]_B}{V_{Cyt}} \qquad (1)$$

where V_X represents the volume of the $X = S$ (shell), B (bulk), and cyt (cytosol) respectively.

The P2Y2R formalism used in this model is taken from Li and Renzel (1994). This model considers the biphasic dependence of IP3Rs on intracellular $[Ca^{2+}]$, in addition to being activated by IP3. They are rapidly activated at low $[Ca^{2+}]$ and are inactivated more slowly at elevated $[Ca^{2+}]$. To capture this slow inactivation of IP3Rs, a Hodgkin-Huxley type inactivation variable h is used to modulate the inactivation probability of the IP3Rs along time (Li-Renzel, 1994). In this study, this inactivation variable is split into a bulk and shell components: h_B, h_S (Eqs. (7) and (4)) to account for their respective dependencies on $[Ca^{2+}]_{Cyt.S}$, $[Ca^{2+}]_{Cyt.B}$.

Following Mikolajewicz et al. (2021), the present study expands the Li-Renzel model of IP3R to include IP3 dynamics as a function of time, where its production rate is dependent on [ATP]. With the

addition of the bulk-shell formalism in the model, IP$_3$ concentration ([IP$_3$]) is split into bulk and shell concentrations respectively: [IP$_3$]$_B$, [IP$_3$]$_S$ (as described by Eqs. (6) and (3) respectively).

The P2X7 formalism in this model is identical to that in Mikolajewicz et al. (2021); it follows the 12 state Markov model presented in Khadra et al. (2013). In brief, the model takes into consideration the different conformations of the P2X7 receptor, including the closed, open, and sensitized states (see appendix for more details). Equations (9) – (11) and the term-by-term analysis of the fluxes and variables are also detailed in the appendix.

Schematic of Cell with Relevant Fluxes
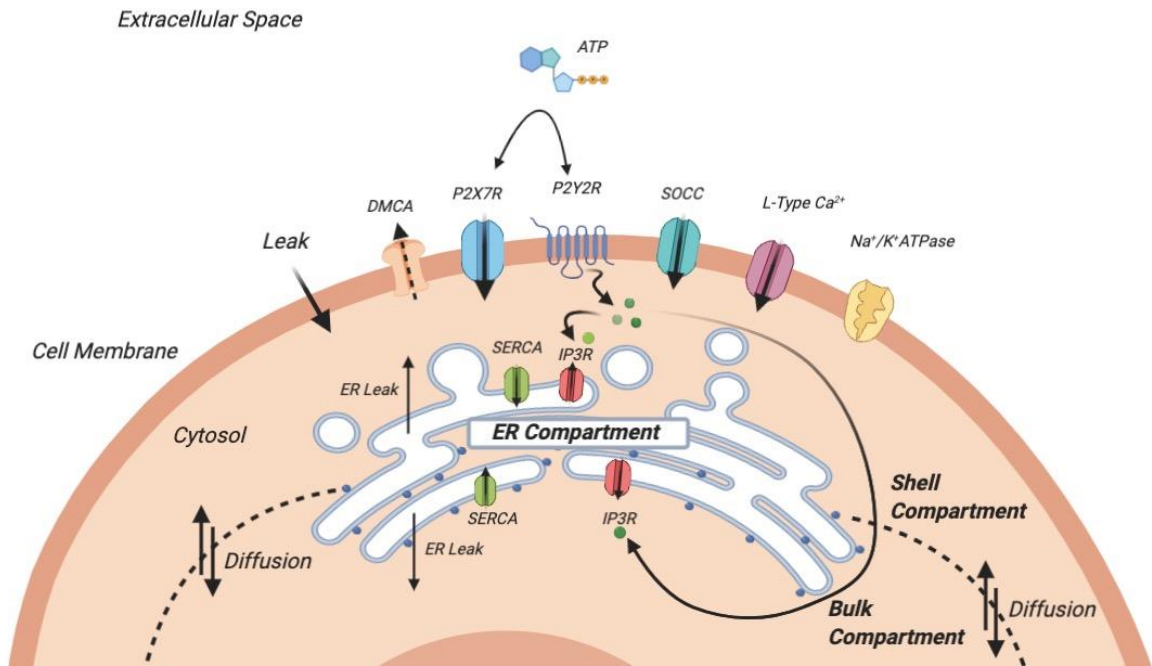
Figure 1: Diagram of the model summarizing the main components of the Ca^{2+} handling. The cell is split into the cytosolic bulk and shell, as well as ER compartment. Ca^{2+} may flux into the cell through an inward leak current and through the P2X7R, SOCC, L-Type channels. Efflux of Ca^{2+} out of the cytosol to the extracellular medium/ER is controlled by the PMCA/SERCA pumps, respectively, while movement of Ca^{2+} between the shell and bulk compartment is mediated by diffusion. IP$_3$Rs and ER drive Ca^{2+} release into the respective cytosolic compartments.

The mathematical model is given by:

(2) $\dfrac{d[Ca^{2+}]_S}{dt}$

$= f * v_s(J_{InLeak} + J_{IP3R-S} + J_{ERLeak-S} - J_{SERCA-S} - J_{Ca-diff} \ - J_{PMCA-S} + J_{P2X7R-Ca}$
$+ J_{SOCC} + J_{J_{L-Type}})$

(3) $\dfrac{d[IP3]_S}{dt} = v_s(\alpha_{ATP} \dfrac{[ATP]}{[ATP] + k_{ATP}} - \delta_{ATP}[IP3]_S - J_{IP3-diff})$

(4) $\dfrac{dh_S}{dt} = \dfrac{h_{\infty S} - h_S}{\tau_{h-S}}$

(5) $\dfrac{d[Ca^{2+}]_B}{dt} = f * v_B(J_{IP3R-B} + J_{ERLeak-B} - J_{SERCA-B} + J_{Ca-diff})$

(6) $\dfrac{d[IP3]_B}{dt} = v_B(J_{IP3-diff} - \delta_{ATP}[IP3]_S)$

(7) $\dfrac{dh_B}{dt} = \dfrac{h_{\infty B} - h_B}{\tau_{h-B}}$

(8) $\dfrac{d[Ca^{2+}]_{ER}}{dt} = f_{ER}v_{ER}(J_{SERCA-S} + J_{SERCA-B} - J_{IP3R-S} - J_{IP3R-B} - J_{ERLeak-S} - J_{ERLeak-B})$

(9) $\dfrac{dm_L}{dt} = \dfrac{m_{\infty L} - m_L}{\tau_L}$

(10) $\dfrac{d[Na]_i}{dt} = J_{P2X7R-Na} - 3 * (1000)J_{NaK}$

(11) $\dfrac{d[K]_i}{dt} = 2 * (1000)J_{NaK} + J_{P2X7R-K},$

Simulations and clustering analysis

The mathematical simulations of the ODEs are run using MATLAB, with the ode15s solver. Ode15s

allows for stiff differential equations to be solved numerically. In order to depict the resting state of the

cell, all simulations are run for 2000 seconds prior to ATP exposure. With no ATP initially, the

concentration of IP3 is assumed to be 0.

The clustering analysis is performed using an R script which divided calcium response signals into groups based on similar features. A hierarchal clustering analysis is used from the R library WGCNA. The level of smoothing is chosen to eliminate homogenous noise from the calcium response signals, while maintaining the presence of the superimposed (fast) oscillations. Each cluster is also quantified by which [ATP] doses predominately produced its signals. To further elucidate the characteristics of the signals within the clusters, a calcium parametrizer algorithm is employed using MATLAB (Mackay et al., 2016). This algorithm takes a calcium signal and systematically quantifies several relevant parameters such as maximum amplitude, time of onset(s), and number of oscillations. Once each Ca^{2+} signal's parameters are quantified, they are averaged, and the variance/standard deviation is computed for each cluster; this allows for seamless quantitative comparisons across clusters. The presence of superimposed oscillations is determined by visual inspection.

Results

Shell Calcium underlies fast oscillations while bulk calcium underlies slow oscillations

To verify if the addition of a bulk and shell formalism into the osteoblastic model is critical in modelling the superimposed (fast) oscillations, we plot in Figure 2 the Ca^{2+} responses at [ATP] = 1000 uM in the shell compartment, the bulk compartment, and in the total cytosolic compartment. The Ca^{2+} response pattern of the shell compartment exhibits a strong: high frequency, high amplitude spiking behavior, which when normalized due to volume considerations (Eq. 1), appears to contribute to the amplitude of the superimposed oscillations (high frequency, low amplitude) seen in the cytosolic Ca^{2+} time series. The Ca^{2+} response in the bulk compartment, on the other hand, exhibits low frequency, high amplitude oscillations which dominate the cytosolic Ca^{2+} response. This analysis validates our hypothesis that the time-scale separation in the cytosolic response is caused by the spatial separation of Ca^{2+} microdomains near the membrane, versus bulk dynamics.

**Simulated Calcium Response Curves of Bulk, Shell, and Cytosol**
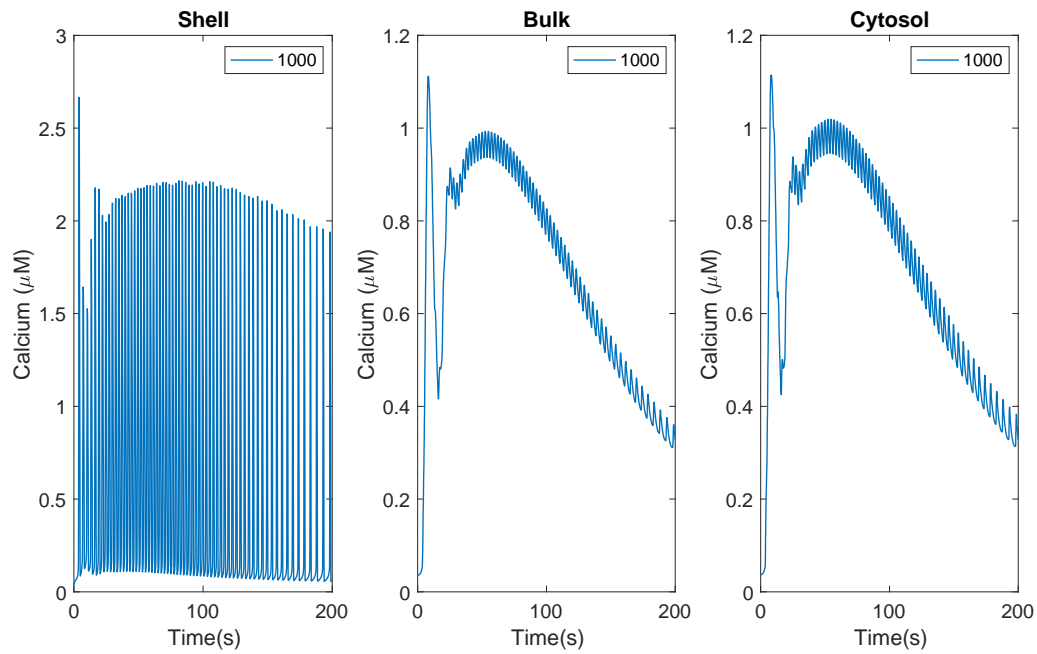
FIGURE 2: Time series simulations of Ca^{2+} in each compartment. In each panel, the graphs plot the concentration of cytosolic Ca^{2+} (in μM) vs. time (in seconds). The leftmost, middle, rightmost panel corresponds to the simulated Ca^{2+} response due to 1000 uM [ATP] in the shell, bulk and cytosol (calculated according to Eq. 1), respectively. Evidently, the shell compartment contributes to an increase in the amplitude of superimposed oscillations in the cytosolic compartment.

Transition from transient to oscillatory to transient behavior in bulk maintained by P2Y2

With the addition of the bulk/shell formalism and numerous fluxes contributing to Ca^{2+} dynamics, one can then verify whether the bulk cytosolic Ca^{2+} response still transitions from transient to oscillatory to transient due to P2Y2 dynamics. Since $[IP_3]_B$ and $[Ca^{2+}]_{ER}$ are slow variables in our system, we can apply a slow-fast analysis by assuming that there is no Ca^{2+} flux through P2X7R and that these variables can be considered parameters. This allows us to plot a two-parameter bifurcation diagram of $[Ca^{2+}]_{ER}$ vs. $[IP_3]_B$, to investigate the possible transient and oscillatory regimes (Figure 3). The P2X7R-knockout system ($J_{P2X7R}= 0$) undergoes two supercritical Hopf bifurcations as $[IP_3]_B$ increases; by extending these Hopf bifurcations to the $[Ca^{2+}]_{ER}$ – parameter space, we obtain the shaded region which represents the oscillatory regime (Figure 3). Figure 3 illustrates that as $[IP_3]_B$ increases, a given solution trajectory

(starting at the red circle and ending at the red star) transitions from regimes that are transient, to

oscillatory, to transient while $[Ca^{2+}]_{ER}$ decreases.

$[Ca^{2+}]_{ER}$ vs. $[IP3]_B$ Bifurcation Diagram
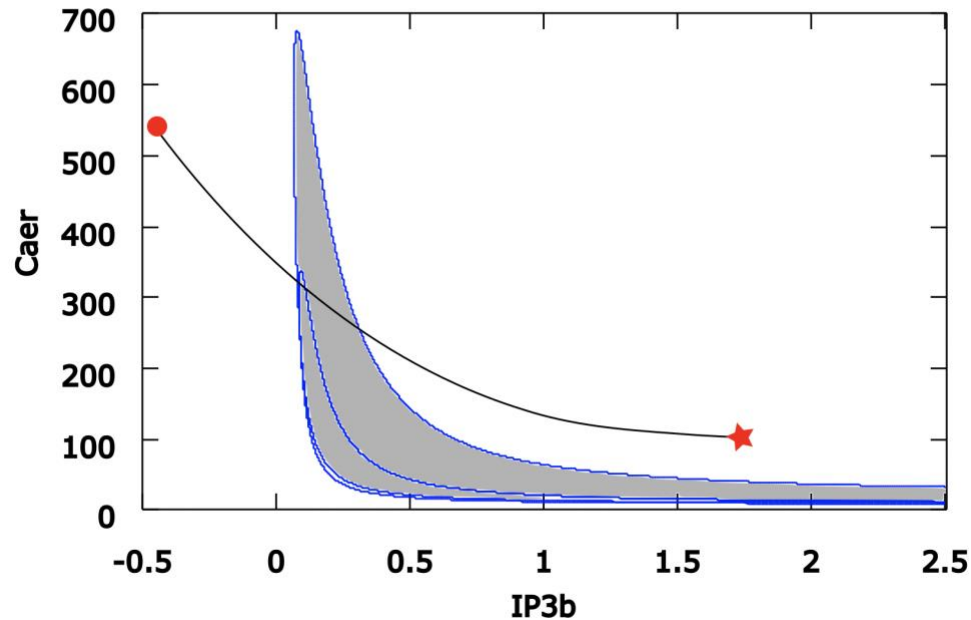
Figure 3. Two parameter bifurcation diagram of $[Ca^{2+}]_{ER}$ vs. $[IP_3]_B$. The grey region represents the oscillatory regime.

Evidently, as solution trajectories start at the red circle and end at the red star, they transition from transient to oscillatory to

transient dynamics. When this solution trajectory avoids the grey regime, it results in a completely transient response.

Clustering analysis results

The clustering analysis performed by the R script produces 21 different clusters of cytosolic calcium

responses, where each cluster ranges from 30 to 169 individual calcium response signals. The [ATP] for

each cluster typically ranges at either low (0.01, 0.1 uM), middle (1, 10 uM), or high (100, 1000, 10 000

uM) [ATP] doses. The superimposed (fast) oscillations are present on 13/21 of the clusters. Table 2

summarizes each cluster's quantified parameters, their [ATP] dose range, and if they exhibit

superimposed (fast) oscillations.

The 6 clusters: M1.turquoise, M4.yellow, M11.greenyellow, M14.black, M18.lightgreen, and

M20.red are chosen for further analysis. All of these clusters exhibit fast oscillations excluding M18. The

cluster M4 is associated with low [ATP] dosages, the clusters M1 and M14 with middle [ATP] dosages,

while M11, M18, and M20 with high [ATP] dosages. The clusters associated with high [ATP] dosages

achieve the highest amplitudes on average, while the clusters associated with middle [ATP] dosages

typically exhibit the greatest number of large-scale oscillations (slow).

Model accurately depicts clusters

We establish that the results provided by the new model accurately reproduce the clusters of the

experimental data. Figure 4 (a) – (e) shows the simulated cytosolic calcium responses with increasing

[ATP] stimuli (0.1, 1, 10, 100, 1000 uM). Figure 4 (f) – (j) represents the respective cluster of data which

mimic model simulations, paired column-wise according to [ATP] dose. Notably, the model captures the

transition from transient ([ATP] = 0.1uM), to oscillatory ([ATP] = 1uM), to transient ([ATP] = 10, 100,

1000 uM) dynamics, and it captures the superimposed (fast) oscillations superimposed on the calcium

response curves. These results are captured with the parameter regime given in Table 1 in the appendix,

with only changing the [ATP] stimulus. Figure 4 (n) represents a cluster of data that does not have slow

or fast oscillations and is observed at higher [ATP] concentrations. By lowering the maximal flux rate of

the SERCA pump, the model can accurately generate a response similar to that seen in the cluster of

Figure 4 (m).

Simulated Calcium Response Curves of Cytosol and Associated Cluster
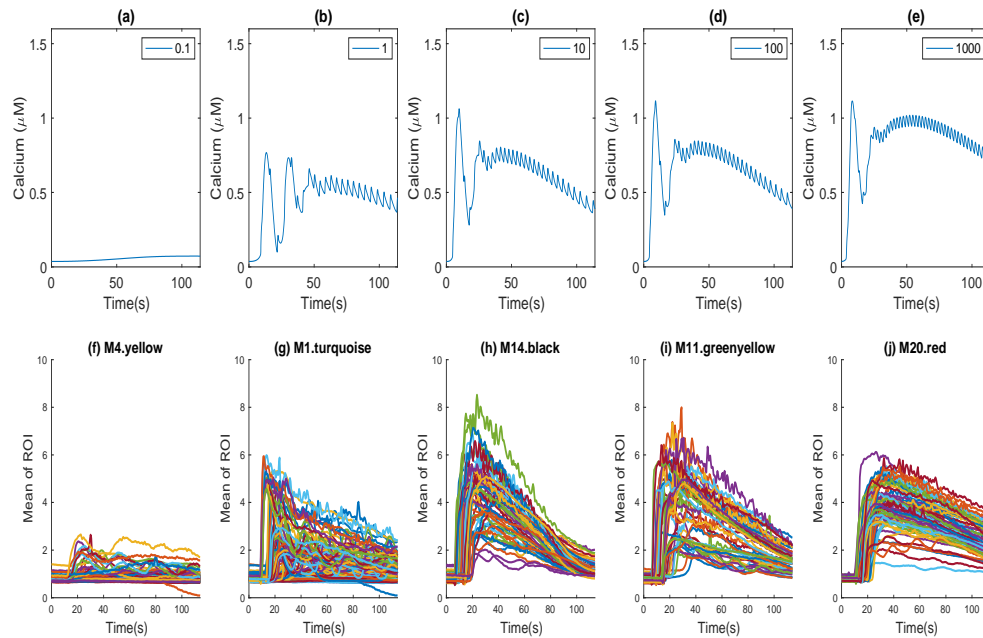
Simulated Calcium Response Curve of Cytosol with SERCA Inhibition and Associated Cluster
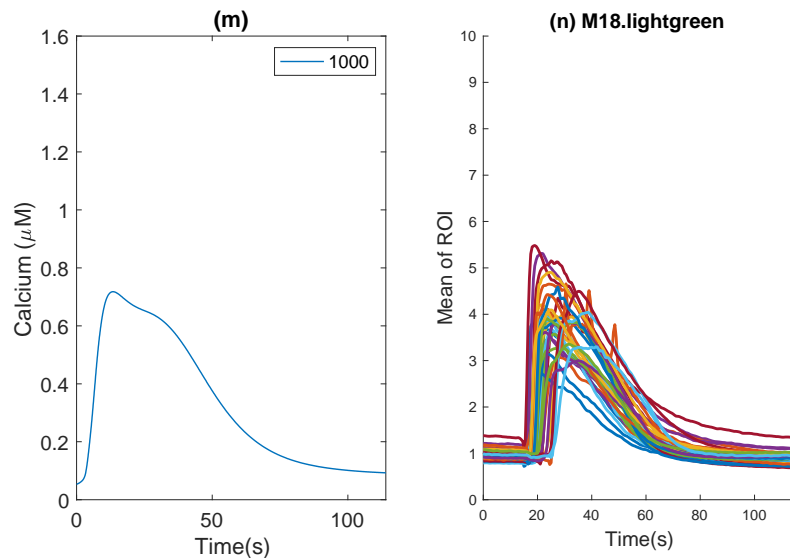
Figure 4 (a) – (j), (m), (n). (a) – (e) Plots of the simulated cytosolic Ca^{2+} responses with increasing [ATP] stimuli (0.1, 1, 10, 100, 1000 uM). (f) – (j) Plots of the 5 clusters which the simulation above can emulate. Evidently, there is a strong correspondence between the simulation and clusters, where the transition between transient to oscillatory to transient and the presence of fast oscillations are both captured. Subplots (m) and (n) represent the simulation with SERCA ; notice how similar the simulation is to the profile of the cluster produced at high ATP concentration.. Evidently, the simulation is successful in reproducing the transient dynamics.

Discussion

Shell calcium underlies fast oscillations while bulk calcium underlies slow oscillations. Previous studies

have implemented a bulk/shell formalism into their models (Lebeau et al., 2000; Lehnert & Khadra,

2019); this has been utilized to provide a clear separation in the $[Ca^{2+}]_i$ time scales in the shell and bulk

compartments, where the shell is much faster than the bulk. The fast dynamics in the shell is achieved

by the numerous plasma membrane fluxes in the shell compartment compared to the bulk compartment;

further, the significantly smaller volume of the shell compartment compared to the bulk compartment

means that higher $[Ca^{2+}]$ may be achieved in the shell. This follows the revised dogma on Ca^{2+} signalling,

where the spatial averaging of these localized, short-lived Ca^{2+} microdomains that exist near the

membrane (shell compartment of cell), towards the center of the cell (bulk compartment of cell),

contributes to Ca^{2+} dynamics (Wang et al., 2004). The clusters which exhibit these fast oscillations are

predicted to be involved in physiological effects that depend on these fast high $[Ca^{2+}]$ events.

Transition from transient to oscillatory to transient behavior in bulk compartment is maintained by P2Y2.

During moderate $[IP_3]_B$ production (i.e. moderate [ATP] stimulus of P2Y2s), the Ca^{2+} released by the

IP_3Rs negatively feedbacks on themselves; this behavior in conjunction with the SERCA pump

counteracting this flux produces the bulk oscillations. During low levels of $[IP_3]_B$ production (i.e. low

[ATP] stimulus of P2Y2s), this negative feedback is lost since Ca^{2+} released by the IP_3Rs is too low,

inducing a transient response. During high levels of $[IP_3]_B$ production (i.e. high [ATP] stimulus of P2Y2s)

the negative feedback is lost because the IP_3Rs become constituently active at high cytosolic $[Ca^{2+}]$; this

also produces a transient response (Li-Renzel, 1994; Smith et al., 2020).

Despite the transition from transient to oscillatory to transient behavior being maintained in the

bulk dynamics, our model exhibits a similar issue to that outlined in Mikolajewicz et al. (2021)'s paper:

our simulation still produces one slow oscillation at high [ATP] when it should be completely transient

(Figure 4d, e). This indicates that the solution to our ODE model remains 'stuck' in the oscillatory regime

at high [ATP], (figure 3, shaded region). Despite this, a large heterogeneity of responses do exist, and our model is representative of certain response curves.

Implications of the model on the clustering analysis data. Our model demonstrates that the addition of a bulk/shell formalism is sufficient in simulating the ATP-induced Ca^{2+} response data for the clusters with fast oscillations: M1.turquoise, M4.yellow, M11.greenyellow, M14.black, and M20.red. The parameters chosen for this model provides some useful biophysical insight into the Ca^{2+} response system (Table 1 in appendix). Firstly, our results reveal that the PMCA, SERCA and diffusion variables are vital in reproducing the superimposed (fast) oscillations, indicating that these fluxes need to be sufficiently fast, while diffusion needs to be sufficiently slow as to not immediately homogenize the shell and bulk compartments. Further, given the low conductance of ions through L-type Ca^{2+} channels, this flux does not contribute significantly to the Ca^{2+} dynamics; this is consistent with the fact that osteoblasts are passive cells (non-spiking).

While our model's simulations produce a slow oscillation at high [ATP] (Figure 4d, e), our results show that it is possible to elucidate which flux is vital in inducing a completely transient response: the SERCA pump. By lowering the maximal flux through the SERCA pump in the model, the slow oscillation at high [ATP] disappears and a truly transient response is generated, capturing the M18.lightgreen cluster's dynamics. However, since this parameter change also abolishes the fast oscillations, and the ability of the model to capture slow oscillations at moderate [ATP] (1, 10 uM) dosages, this parametrization indicates that there is a heterogeneity in the response and one parameter set is not enough to produce all the dynamics observed. Interestingly, the importance of the SERCA pump in producing slow oscillations has been explored experimentally, where hippocampal neurons that are given thapsigargin (SERCA inhibitor) lost their slow oscillations (Korkotian et al., 2011); this aligns with the biophysical prediction of our model.

Future Directions. In order to more accurately capture the spatial phenomena of calcium microdomains, we are exploring the implementation of partial differential equation (PDE) model which models space in

addition to time. This formalism has been shown to be successful in capturing spatially heterogenous dynamics (Fletcher et al., 2009) Further, we are looking into performing an analysis on the images which produced the calcium response curves, to explore whether spatially heterogenous dynamics may be visualized from the experimental data.

APPENDIX

P2X7 dynamics

The kinetics of the P2X7Rs are mathematically constructed based on the Markov model presented in Khadra et al. (2013). This Markov model is chosen as it takes into consideration the desensitization of the receptor (after subsequent depolarization/activation). The model is comprised of twelves states divided into three subcategories (see diagram in Fig. 5 for illustration). The first subcategory, depicted in the middle row of Fig. 5, corresponds to the four naive states of the receptor (C1, C2, Q1 and Q2), defined as not having been previously stimulated by an agonist. The second subcategory, shown in the lower row of Fig. 5, corresponds to the four sensitized states of the receptor (C3, C4, Q3 and Q4), defined as having been previously exposed to the agonist. The third and final subcategory, placed in the upper row of Fig. 5, includes four desensitized states (Di, where i = 1, 2, 3, 4). The 12 states are represented by rectangular boxes, attached to three white or black circles. The black circles represent the occupation of ATP in its binding site on the receptor, while those that are white represent its absence. The P2XR receptor does not show signs of its channel widening of its pore after sensitization (Peverini et al., 2018). As such, it is assumed that the naive and sensitized states possess the same characteristic conductance. It is also assumed that the receptor becomes desensitized faster when more ATP is bound: $H2(C2) < H2(Q1) < H2(Q2)$. Such assumptions have not altered significantly the time series stimulations of P2XR.
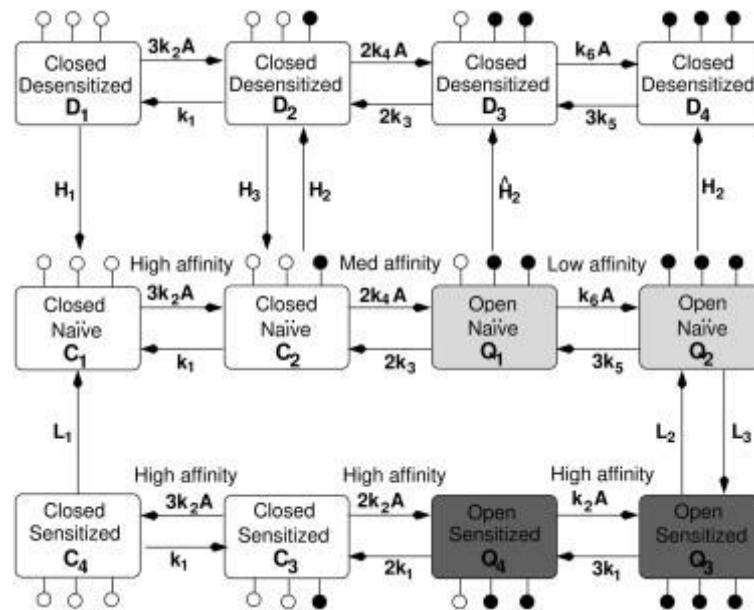
FIGURE 5: Graphical Model of the P2X7R Markov model. The upper row corresponds to receptors in the desensitized state, the middle row to naive receptors, and the lower row to sensitized receptors. The enclosed rectangular boxes represent the P2X7R receptors. Attached to said rectangles are white and black circles. The black circles represent the attachment of ATP to its binding site, whereas the white ones represent the unoccupied binding sites. The receptors identified by Ci and Di, where i = 1,2,3,4, are closed, while the receptors determined by Qi are open. For more specification as to the framework variables, refer to Table 1.

Equations (9)-(11)

An L-type Ca^{2+} channel is introduced into the model as they are expressed by osteoblasts (Grygorczyk et al., 1989). L-type Ca^{2+} is voltage-gated channel whose kinetics can be assumed to follow the Hodgkin Huxley formalism, with m_L (equation (9)) representing its activation variable along time (Zeng et al., 2009). Since the L-type Ca^{2+} channel and its gating variable are voltage dependent, a modified Goldman-Hodgkin-Katz (GHK) formalism is introduced to continuously determine the voltage based on the present intracellular ionic concentrations. In contrast to the original GHK equation, the modified version accounts for currents carried by divalent ions, and the effects of the unstirred layer and the peri-axonal space (Chang, 1983).

Since P2X7Rs are non-specific cation channels, sodium (Na^+) and potassium (K^+) may flux through these receptors when their gating opens in response to extracellular ATP. This may impact

intracellular Na^+ and K^+ concentrations, and hence contribute to changes in measured voltage. To account for this, intracellular concentrations of Na^+ ($[Na]_i$) and K^+ ($[K]_i$) dynamics are modelled (Eqs. (10) and (11)). An Na/K ATPase is included in the model by following the formalism used in Gin et al. (2007); the Na/K ATPase functions to counteract the Na^+ and K^+-P2X7R fluxes and establish a physiological equilibrium.

Definition of fluxes in equations (2) – (11)

Ca^{2+} buffering is included in the model by considering the fraction of free Ca^{2+} concentration f < f$_{ER}$ <<1 (Mikolajewicz, Smith, Komarova and Khadra, 2021). J$_{InLeak}$ is the constant inward flux through the plasma membrane, J$_{IPR-S}$/ J$_{IPR-B}$ is the flux through the IP$_3$R in the shell/bulk compartment, J$_{ERLeak-S}$ /J$_{ERLeak-B}$ is the leak flux from the ER to the shell/bulk compartment, J$_{SERCA-S}$ /J$_{SERCA-B}$ is the flux across the SERCA pumps from the cytosol to the ER, J$_{Ca-diff}$ is the diffusion of Ca^{2+} across the shell/bulk compartments, J$_{PMCA-S}$ is the flux across the plasma membrane via PMCA pumps, J$_{P2X7-Ca}$ is the Ca^{2+} flux across P2X7Rs, J$_{SOCC}$ is the flux across store operated Ca^{2+} channels, J$_{L-Type}$ is the flux across L-type Ca^{2+} channels, α_{ATP} is the maximum rate of IP$_3$ production by P2Y2Rs in response to ATP, K$_{ATP}$ is the half maximal production of IP$_3$ by P2Y2Rs in response to ATP, δ_{ATP} is the rate of degradation for IP$_3$, J$_{IP3-diff}$ is the diffusion of IP3 across the shell/bulk compartments, $h_{\infty S}$/$h_{\infty B}$ is the steady state of IP3R inactivation by Ca^{2+} in the shell/bulk compartments, τ_{h-S}/τ_{h-B} is the time constant of IP$_3$R inactivation in the shell/bulk compartments, $m_{\infty L}$ is the steady state of L-type Ca^{2+} channel opening probability, τ_L is the time constant of L-type Ca^{2+} channel opening, J$_{P2X7-Na}$ is the Na^+ flux across P2X7Rs, J$_{P2X7-K}$ is the K^+ flux across P2X7Rs, and J_{NaK} is the flux due to the Na/K ATPase pumping 2 K^+ in per 3 Na^+ out. The factors v$_s$, v$_B$, v$_{ER}$ represent the ratio: V$_{cytosol}$/V$_X$ where X = S (shell), B (Bulk), and ER, respectively. Detailed descriptions of the flux terms, diffusion terms, voltage formalism, and Na/K ATPase is provided in the following section.

Additional details about the Ca^{2+} flux terms and other aspects of the model

IP$_3$R Ca^{2+} Flux

The IP$_3$R flux is modelled by the equation:

$$J_{IP3R-X} = v_{IP3R}O_{IP3R}([Ca^{2+}]_{ER} - [Ca^{2+}]_X),$$

where v$_{IP3R}$ is the maximum rate of Ca^{2+} flux through IP$_3$Rs, X = S (shell) or B (bulk) depending on the compartment which the IP$_3$Rs are fluxing into, and O$_{IP3R}$ is the open probability of the IP$_3$Rs, given by:

$$O_{IP3R} = m_\infty^3 n_\infty^3 h^3$$

Where m, n, h are the Hodgkin Huxley type gating variables representing IP$_3$ binding, activation by [Ca^{2+}]$_X$, and inactivation by [Ca^{2+}]$_X$ respectively (De Young & Keizer, J., 1992).

According to the Li-Renzel formalism (1994) implemented in this model, the time scales of IP$_3$ binding and activation by [Ca^{2+}]$_X$ are significantly faster than the inactivation by [Ca^{2+}]$_X$, hence a steady state approximation can be applied such that m and n are at their respective steady state equilibria:

$$m_\infty = \frac{[IP_3]_X}{[IP_3]_X + d_1} \qquad n_\infty = \frac{[Ca^{2+}]_X}{[Ca^{2+}]_X + d_5}$$

where X = S (shell) or B (bulk) and d$_i$ (i = 1, 2, 3, 4, 5) refers to the dissociation constants determined by De Young and Keizer once having fit Bezprozvanny et al. (1991)'s experimental data.

For the Hodgkin Huxley type gating variable h, which is not at dynamic equilibrium, the time constant and steady state value is given by:

$$\tau_{h-X} = \frac{1}{a_2(Q_2 + [Ca^{2+}]_X)} \qquad h_{\infty X} = \frac{Q_2}{Q_2 + [Ca^{2+}]_X} \qquad Q_2 = d_2\frac{[IP_3]_X + d_1}{[IP_3]_X + d_3}$$

ER Ca^{2+} Leak

A Ca^{2+} leak flux from the ER into the cytosolic shell or bulk (X = S or B respectively) is modelled following Li-Renzel's model (1994):

$$J_{ERLeak-X} = v_{ERLeak}([Ca^{2+}]_{ER} - [Ca^{2+}]_X)$$

Where v_{ERLeak} refers to the maximum leak rate of Ca^{2+}.

Ca²⁺ ATPase Activity

The two Ca^{2+} ATPases are modelled as hill functions (Cao et al., 2014; Croisier et al., 2013): the SERCA pump which re-uptakes Ca^{2+} into the ER, and the PMCA pump which extrudes Ca^{2+} from the cell.

$$J_y = v_y \frac{[Ca^{2+}]_X^2}{[Ca^{2+}]_X^2 + k_y^2}$$

where y = SERCA-X or PMCA-X, v_y = refers to the respective maximal rates of pump activation and k_y represents the affinity of the respective pumps for Ca^{2+}. For y = SERCA-X, X = S (shell) or B (bulk) depending on which region the Ca^{2+} re-uptake is occurring. For y = PMCA, X = S (shell) only since the PMCA pump is a membrane receptor.

Plasma Membrane Ca²⁺ Leak

A small Ca^{2+} inward leak across the plasma membrane is assumed to exist. This primarily assisted in keeping the Ca^{2+} concentration positive inside the cell in the absence of ATP.

P2X7R Ca²⁺ / Na⁺ / K⁺ Fluxes

Before calculating flux, Khadra et al.'s 2013 Markov model is used to calculate the current produced by the P2X7R:

$$I_{P2X7R} = g_{X7}(Q_1 + Q_2 + Q_3 + Q_4)(V - E)$$

where g_{X7} is the conductance of P2X7R, Q_i (i = 1-4) are the open states, V is the voltage of the cell, and E is the reversal potential (assumed to be zero since P2X7R is non-specific for Ca^{2+}, Na^+, K^+).

To convert this current into a flux, the Zeng et al. (2009) formalism is used. Since P2X7Rs are non-specific, this flux is multiplied by the fraction of which each cation: Ca^{2+}, Na^+, K^+, fluxes through (Egan & Khakh, 2004). The resulting three P2X7R fluxes are:

$$J_{P2X7R-\beta} = -f_\beta \frac{I_{P2X7R}}{zFV_{osteo}}$$

Where $\beta = Ca^{2+}$, Na^+, K^+; f_β refers to the fraction of flux of the respective cation through P2X7, z is the valence of either +1 (Na^+, K^+) or +2 (Ca^{2+}), F is Faraday's constant, and V_{osteo} is the volume of the osteoblast in litres.

Diffusion of Ca^{2+} and IP_3 Between Shell and Bulk

The diffusion of Ca^{2+} and IP_3 between Shell (S) and Bulk (B) is modelled as being proportional to the concentration differences between these compartments, following (Cao et al., 2014)'s formalism:

$$J_{Ca-Diff} = v_{Ca}([Ca^{2+}]_S - [Ca^{2+}]_B)$$

$$J_{IP3-Diff} = v_{IP3}([IP3]_S - [IP3]_b)$$

where v_{Ca}, v_{IP3} represent the maximal diffusion rate between the shell and bulk for Ca^{2+} and IP_3 respectively.

Store-Operated Ca^{2+} Channel (SOCC)

SOCCs are channels on the plasma membrane that are activated when ER Ca^{2+} stores are reduced, which subsequently allows Ca^{2+} entry. See (Putney et al., 2016) for more details on SOCC.

Using the formalism from (Cao et al., 2014), this flux is modelled as a fourth order reverse Hill function:

$$J_{SOCC} = v_{socc}(\frac{k_{SOCC}^4}{k_{SOCC}^4 + [Ca^{2+}]_{ER}^4})$$

Where v_{SOCC} is the maximal flux through the SOCCs, and k_{SOCC} represents the Ca_{ER}^{2+} concentration when the half-maximal flux rate is achieved.

Voltage Formalism

We incorporate the modified Goldman-Hodgkin-Katz (GHK) formalism (Chang, 1983). This allows us to continuously determine the voltage based on the present intracellular ionic concentrations. In contrast to the original GHK equation, the modified version accounts for currents carried by divalent ions, and the effects of the unstirred layer and the peri-axonal space. This is given by the following equation:

$$V = \frac{RT}{F} \ln \left(\frac{P_k[K]_o + P_{Na}[Na]_o + 4P_{Ca}[Ca]_o + \frac{y_k J_k P_K}{P_{DK}}}{P_K[K]_i + P_{Na}[Na]_i + 4P_{Ca}[Ca]_S} \right)$$

where V is the calculated voltage, R is the ideal gas constant, T is the temperature in Kelvin, F is faradays constant, P_X (X = K, Na, Ca) are the relative permeabilities of the ions. K, Na, Ca and their subscripts o/i represent the extracellular and intracellular concentrations respectively; the subscript S for $[Ca^{2+}]_S$ refers to the shell Ca^{2+}.

Note that we assume all extracellular concentrations to be constant at their normal physiological concentrations, while the intracellular concentration dynamically vary.

L-Type Ca^{2+} Channel

The formalism for the L-Type Ca^{2+} channel is taken from Zeng et al. (2009). Before converting to a Ca^{2+} flux, they first determine the current through the channels:

$$I_L = g_L m_L h_{\infty L} (V - E_{Ca})$$

where g_L is the conductance through L-Type channels, V is the calculated voltage of the cell, and E_{Ca} is the reversal potential for Ca^{2+} given by the Nernst equation:

$$E_{Ca} = \frac{RT}{zF} \ln \left(\frac{[Ca]_o}{[Ca]_S} \right)$$

where R is the ideal gas law constant, T is the temperature in Kelvin, z is the valence of +2, and F is faradays constant.

m_L and $h_{\infty L}$ are the Hodgkin Huxley type gating variables representing activation and deactivation of L-Type channel respectively. $h_{\infty L}$ (i.e. deactivation) is rapid and assumed to be at steady state, where:

$$h_{\infty L} = \frac{0.00045}{0.00045 + [Ca^{2+}]_S}$$

Meanwhile, m_L (i.e. activation) dynamically varies, with the time constant and steady state value given by:

$$m_{\infty L} = \frac{1}{1 + e^{\frac{-(V+50)}{3}}} \qquad \tau_L = 18e^{-(\frac{V+45}{20})^2} + 1.5$$

Where V is the calculated voltage of the cell.

To convert this current into a Ca^{2+} flux, the formalism from Zeng et al. (2009) is adopted where

$$J_{L-Type} = -\frac{I_L}{zFV_{osteo}}$$

where z is the valence (+2), F is faradays constant, and V_{osteo} is the volume of the cell.

Na/K ATPase

The flux through the Na/K ATPase follows (Gin et al., 2007) formalism, where we implement the 4 state

Na/K model developed by (Smith & Crampin, 2004). This model was originally 15 states (Borlinghaus,

Apell, & Läuger, 1987) until Smith and Crampin reduced it to 4. The whole-cell pump flux density is

given by

$$J_{NaK} = \alpha_{NaK}v_{NaK}$$

Where α_{NaK} is the density of the Na-K ATPase and where v_{NaK} is given by

$$v_{NaK} = \frac{\alpha_1^+ \alpha_2^+ \alpha_3^+ \alpha_4^+ - \alpha_1^- \alpha_2^- \alpha_3^- \alpha_4^-}{\Sigma}$$

where the α_i^+ are the forward step reactions and α_i^- are the backward step reactions for values of i=1-4.

Details regarding the values of α, Σ, thermodynamic considerations and voltage dependent partitioning

can be found in (James Sneyd)'s Table 1 and Appendix A, as well as in Smith and Crampin(2004).

Table 1 Parameter Values of O.D.E. Model

Buffering and Scaling		
f	0.01	Cytosolic Calcium Buffering
f_{ER}	0.025	ER Calcium Buffering
v_S	48	Cytosol/Shell Volume Ratio
v_b	1	Cytosol/Bulk Volume Ratio
V_{ER}	9.4	Cytosol/ER Volume Ratio
Plasma Membrane Fluxes		
J_{INLeak}	0.15 uM s^{-1}	Inward Ca^{2+} Leak (Passive)
V_{PMCA}	8 uM s^{-1}	Maximal PMCA Flux
k_{PMCA}	0.1 uM	PMCA Calcium Affinity

V_{socc}	1.6 uM s^{-1}	Maximal SOCC Flux
k_{socc}	100 uM	SOCC Calcium Affinity
ER Fluxes		
V_{SERCA}	30 uM s^{-1}	Maximal SERCA Flux
k_{SERCA}	0.105 uM	SERCA Calcium Affinity
V_{ERLeak}	0.03 s^{-1}	Rate of Ca^{2+} across ER
Li-Renzel IP$_3$R Model		
d_1	0.13 uM	IP$_3$ dissociation Constant (Ca^{2+} unbound from inactivation site)
d_2	1.049 uM	Ca^{2+} dissociation constant from the inactivation site (IP$_3$ bound)
d_3	0.9434 uM	IP$_3$ dissociation constant (Ca^{2+} bound to inactivation site)
d_5	0.08234 uM	Ca^{2+} dissociation constant from activation site
a_2	0.2 uMs^{-1}	Ca^{2+} binding rate to inactivation site
V_{IP3R}	15 uMs^{-1}	Maximal IP$_3$R Flux
P2X7R Model		
g_{X7}	7.5*10^{-9} S	P2X7R conductance of both naïve and sensitized states
E	0 mV	Reversal Potential
k_1	0.3 s^{-1}	Transition Rates between States (same row)
k_2	1265 M^{-1}s^{-1}	
k_3	2.4 s^{-1}	
k_4	1581 M^{-1}s^{-1}	
k_5	1.58 s^{-1}	
k_6	221 M^{-1}s^{-1}	
L_1	0.0001	Transition rates between naïve (middle) and sensitized (bottom) rows
L_2	0.004	
L_3	0.05	
H_1	0.001	Transition rates between naïve (middle) and desensitized (upper) rows
$H_{2(C2)}$	0.01	
$H_{2(Q1)}$	0.1	
$H_{2(Q2)}$	0.6	
f_{Ca}	0.046	Percentage of P2X$_7$R Flux that is Ca^{2+}
f_{Na}	0.477	Percentage of P2X$_7$R Flux that is Na^+
f_K	0.477	Percentage of P2X$_7$R Flux that is K^+
V_{Osteo}	6.5 pL	Volume of Osteoblast

IP$_3$ Dynamics		
α_{ATP}	0.03 uMs^{-1}	Maximal IP$_3$ Production
k$_{ATP}$	1 uM	Sensitivity of IP$_3$ production to [ATP]
δ_{ATP}	0.01 s^{-1}	Degradation Rate of IP$_3$
Voltage Formalism		
F	96485 C mol^{-1}	Faradays Constant
R	8.314 J mol^{-1} K^{-1}	Ideal Gas Constant
T	300 K	Temperature
K$_o$	4 mM	Extracellular K$^+$ Concentration
Na$_o$	140 mM	Extracellular Na$^+$ Concentration
Ca$_o$	2 mM	Extracellular Ca^{2+} Concentration
P$_{Ca}$	35	Ca^{2+} Permeability
P$_K$	30	K$^+$ Permeability
P$_{Na}$	1	Na$^+$ Permeability
L-Type Ca^{2+} Formalism		
F	96485 C mol^{-1}	Faradays Constant
R	8.314 J mol^{-1} K^{-1}	Ideal Gas Constant
T	300 K	Temperature
g$_L$	3.5 * 10^{-12} S	Conductance through L-Type Channels
V$_{Osteo}$	6.5 pL	Volume of Osteoblast
Ca$_o$	2 mM	Extracellular Ca^{2+} Concentration
Diffusion Formalism		
v$_{Ca}$	7 s^{-1}	Rate of Diffusion from Bulk to shell of Ca^{2+}
V$_{IP3}$	7 s^{-1}	Rate of Diffusion from Bulk to shell of IP$_3$
NaK ATPase Formalism		
α_{NaK}	2200 um^{-2}	Density of ATPases on Membrane
Details regarding the rest of the values can be found in (James Sneyd)'s Table 1 and Appendix A, as well as in Smith and Crampin(2004).		

Table 2 Parametrization of Clusters. Definitions of parameters can be found in (Mackay et al., 2016)

Clusters	Amplitude (A.U)	Time of Onset(s)	Activation Time(s)	FWHM (s)
M1. Turquoise	1.646822013	17.18181818	4.5491481	23.89187418
M2.tan	0.03937084	35.28571429	19.47313237	47.4211446
M3.cyan	0.040743964	43.22222222	14.18152031	33.53014417

M4.yellow	0.0175587	57.5	10.82457909	25.48976711
M5.green	2.149073065	14.91509434	3.86117362	14.75214521
M6.purple	1.027650805	27.625	17.43119266	25.03451289
M7.grey60	3.078590714	16.44117647	3.128825842	30.94549379
M8.brown	4.907107488	16.01162791	4.164954738	35.84687129
M9.midnightblue	2.845101528	15.52564103	4.579359478	39.21571395
M10.royalblue	2.537757252	16.86538462	5.183385422	24.50710757
M11.greenyellow	2.781650929	13.51388889	5.167103539	35.4890782
M12.lightcyan	2.562711812	17.5483871	4.088859764	26.81913499
M13.magenta	2.442327995	17.625	4.627047837	17.89809961
M14.black	3.284764771	11.40909091	4.610890027	41.01174789
M15.lightyellow	2.38319147	18.4	5.810397554	46.11629533
M16.blue	2.976471924	15.8877551	6.091261668	43.03065237
M17.salmon	3.384014667	17.24358974	3.53731895	33.18183957
M18.lightgreen	3.115695034	18.28787879	3.211565193	26.43202669
M19.darkred	2.800143299	18.37931034	2.919510101	25.23830614
M20.red	2.772416012	15.55405405	7.27129751	41.24664376
M21.pink	2.527660375	13.85	7.246395806	46.33584535

Clusters	Area under curve	Decay time(s)	# of Oscillations	Mag. Of Oscillations
M1. Turquoise	53.6296964	38.35153325	4.756756757	0.446873754
M2.tan	2.007601732	66.71271332	3.166666667	0.024504578

M3.cyan	1.876043711	37.93747598	2.8	0.018084219
M4.yellow	0.512163459	44.35047852	4.3	0.02259506
M5.green	43.04973094	10.40666591	4.12244898	0.523022446
M6.purple	32.95987935	16.74813622	6.333333333	0.046173772
M7.grey60	102.4806303	22.39001489	2.769230769	0.723994514
M8.brown	108.3891187	25.57429237	2.693548387	0.594626959
M9.midnightblue	117.298855	42.22473033	3.1875	0.518448862
M10.royalblue	74.10453707	16.9406053	3.909090909	0.353157062
M11.greenyellow	110.4974935	77.28133259	3.838709677	0.547116774
M12.lightcyan	76.909726	43.36340006	4.678571429	0.486053464
M13.magenta	50.55007926	25.0368506	4.3	0.533202043
M14.black	139.2599829	83.95685352	3.127659574	0.664611408
M15.lightyellow	113.7582084	101.1601932	3.08	0.449974257
M16.blue	131.2553074	47.17774486	3	0.565166096
M17.salmon	119.2839361	21.02564103	2.516129032	0.601589905
M18.lightgreen	86.50120302	16.26631345	2.827586207	0.537628575
M19.darkred	74.86313995	13.75862069	2.72	0.454524616
M20.red	109.4710895	115.2343702	3.482758621	0.41199385
M21.pink	119.911473	108.4794231	2.935483871	0.460214276

Clusters	Period(s)	Period std. (s)	FWHM of Osc.	Persistence of Osc.
M1. Turquoise	24.8230243	7.284842376	8.492355284	77.09459459

M2.tan	27.8722222	6.499758193	9.463371074	48.83333333
M3.cyan	35.6333333	8.270012806	10.03410924	54.2
M4.yellow	30.2110994	5.656655108	8.785371682	57.4
M5.green	30.4496396	10.25698801	9.227318035	69.8877551
M6.purple	13.3333333	5.674812066	5.310458116	70.83333333
M7.grey60	46.8919872	6.226039195	13.86349966	71.03846154
M8.brown	41.6023224	10.38030496	14.50506764	60.87096774
M9.midnightblue	37.7039931	8.284591301	13.44946605	67.5
M10.royalblue	26.5386905	10.78845621	9.967291153	69.22727273
M11.greenyellow	29.2344662	9.207225256	10.96406357	65.67741935
M12.lightcyan	21.0169218	5.158239432	9.108300555	70.76785714
M13.magenta	26.8096825	8.879541841	8.967287806	74.65
M14.black	40.145179	9.66610989	13.31097838	69.42553191
M15.lightyellow	32.797	11.5281525	14.58371922	58.26
M16.blue	40.2488306	8.898543021	15.09869678	65.475
M17.salmon	46.1518817	12.90565092	17.1899537	68.62903226
M18.lightgreen	43.2444581	10.08647343	13.55022702	66.32758621
M19.darkred	39.2916667	8.355390008	15.37560713	61.46
M20.red	27.7204816	10.60768218	14.63181282	56.81034483
M21.pink	35.3481183	8.57597799	15.34787322	64.83870968

Clusters	Duty Cycle	# of Osc. (Coherent)	Mag. Of Osc. (Coherent)	Period (Coherent)

M1. Turquoise	0.371549271	3.720588235	0.452148336	24.83954328
M2.tan	0.461434573	3	0.024327371	10.70833333
M3.cyan	0.28641058	2.333333333	0.019339849	34.05
M4.yellow	0.337473187	3.571428571	0.024367167	31.12068289
M5.green	0.332178404	3.195121951	0.52910911	31.98719512
M6.purple	0.39054104	5	0.040249651	12.15277778
M7.grey60	0.316742554	2.434782609	0.769795625	49.58768116
M8.brown	0.412558019	2.320754717	0.640548011	46.2172956
M9.midnightblue	0.481472476	2.933333333	0.512973216	39.53263889
M10.royalblue	0.402172334	3.409090909	0.354274588	26.10429293
M11.greenyellow	0.413433635	2.965517241	0.527870233	29.73881363
M12.lightcyan	0.432819087	3.875	0.468966312	20.26001984
M13.magenta	0.352453327	3.291666667	0.642943744	28.08078704
M14.black	0.490422839	2.608695652	0.674107545	41.31086957
M15.lightyellow	0.542069731	2.761904762	0.459168805	39.7202381
M16.blue	0.5328575	2.642857143	0.563554942	41.23402211
M17.salmon	0.381487317	2.3	0.60588238	48.59166667
M18.lightgreen	0.340078052	2.458333333	0.55221953	48.75545635
M19.darkred	0.391953253	2.5	0.472319566	40.46780303
M20.red	0.558487522	2.666666667	0.475216261	28.55809083
M21.pink	0.499345109	2.607142857	0.49856784	37.61011905
Clusters	**Period Std. (Coherent)**	**FWHM of Osc. (Coherent)**	**Persistence of Osc. (Coherent)**	**Duty Cycle (Coherent)**

Clusters	Number of Deviation Peaks	Presence of Superimposed Osc.(Y/N)	[ATP] Dose Range
M1. turquoise	3.924216114	8.384404098	51.54411765	0.372714498
M2.tan	1.033593686	5.560537112	21	0.4753029
M3.cyan	5.113791863	9.607674276	41.33333333	0.289276099
M4.yellow	3.83075227	7.908544748	51.14285714	0.336640536
M5.green	5.271912802	9.019097032	49.86585366	0.332753664
M6.purple	2.956761388	5.159470585	49.33333333	0.413263983
M7.grey60	4.869517642	14.20045432	63.43478261	0.316544972
M8.brown	6.697992143	15.17520411	57.97169811	0.41096149
M9.midnightblue	8.798215299	13.04503959	66.55	0.407782836
M10.royalblue	7.758097811	10.05963535	54.25	0.444776125
M11.greenyellow	3.702454889	11.49627024	46.9137931	0.465114494
M12.lightcyan	2.556439157	9.105739747	46.91666667	0.472713005
M13.magenta	6.825106105	9.078120855	60.14583333	0.340573398
M14.black	7.631244197	13.70755273	60.20652174	0.527866608
M15.lightyellow	4.598434524	15.41340992	51.04761905	0.48470545
M16.blue	6.663025358	15.13833651	60.67142857	0.57815043
M17.salmon	9.316469627	17.21059989	64.03333333	0.382227942
M18.lightgreen	5.399971165	14.10450632	59.75	0.347888132
M19.darkred	7.164642831	15.95621755	57.97727273	0.465711009
M20.red	4.80224404	14.84315837	40.24074074	0.625250733
M21.pink	6.229641234	15.31145977	60.16071429	0.482346025

M1. turquoise	4.657894737	Y	Middle
M2.tan	3.166666667	N	Low
M3.cyan	2	N	Low
M4.yellow	3.384615385	N	Low
M5.green	3.886792453	N	Middle
M6.purple	6.333333333	N	Low
M7.grey60	2.352941176	Y	Middle
M8.brown	2.220930233	Y	High
M9.midnightblue	2.794871795	Y	High
M10.royalblue	3.461538462	Y	Middle
M11.greenyellow	3.444444444	Y	High
M12.lightcyan	4.433333333	Y	Middle
M13.magenta	4.09375	Y	Low
M14.black	2.818181818	Y	Middle
M15.lightyellow	2.733333333	N	High
M16.blue	2.612244898	Y	High
M17.salmon	2.205128205	Y	High
M18.lightgreen	2.606060606	N	High
M19.darkred	2.482758621	N	High
M20.red	2.945945946	Y	High
M21.pink	2.5	Y	High

Citations

Bezprozvanny, l., Watras, J. and Ehrlich, B., 1991. Bell-shaped calcium-response curves of lns(l,4,5)P3- and calcium-gated channels from endoplasmic reticulum of cerebellum. *Nature*, 351(6329), pp.751-754.

Borlinghaus, R., Apell, H. and Läuger, P., 1987. Fast charge translocations associated with partial reactions of the Na,K-pump: I. Current and voltage transients after photochemical release of ATP. *The Journal of Membrane Biology*, 97(3), pp.161-178.

Burnstock, G., 2018. Purine and purinergic receptors. *Brain and Neuroscience Advances*, 2, p.239821281881749.

Cao, P., Tan, X., Donovan, G., Sanderson, M. and Sneyd, J., 2014. A Deterministic Model Predicts the Properties of Stochastic Calcium Oscillations in Airway Smooth Muscle Cells. *PLoS Computational Biology*, 10(8), p.e1003783.

Chang, D., 1983. Dependence of cellular potential on ionic concentrations. Data supporting a modification of the constant field equation. *Biophysical Journal*, 43(2), pp.149-156.

Croisier, H., Tan, X., Perez-Zoghbi, J., Sanderson, M., Sneyd, J. and Brook, B., 2013. Activation of Store-Operated Calcium Entry in Airway Smooth Muscle Cells: Insight from a Mathematical Model. *PLoS ONE*, 8(7), p.e69598.

De Young, G. and Keizer, J., 1992. A single-pool inositol 1,4,5-trisphosphate-receptor-based model for agonist-stimulated oscillations in Ca2+ concentration. *Proceedings of the National Academy of Sciences*, 89(20), pp.9895-9899.

Egan, T., 2004. Contribution of Calcium Ions to P2X Channel Responses. *Journal of Neuroscience*, 24(13), pp.3413-3420.

Erb, L. and Weisman, G., 2012. Coupling of P2Y receptors to G proteins and other signaling pathways. *Wiley Interdisciplinary Reviews: Membrane Transport and Signaling*, 1(6), pp.789-803.

Fletcher, P. A., & Li, Y.-X., 2009. An Integrated Model of Electrical Spiking, Bursting, and Calcium Oscillations in GnRH Neurons. *Biophysical Journal*, 96(11), pp. 4514–4524.

Gin, E., Crampin, E., Brown, D., Shuttleworth, T., Yule, D. and Sneyd, J., 2007. A mathematical model of fluid secretion from a parotid acinar cell. *Journal of Theoretical Biology*, 248(1), pp.64-80.

Grygorczyk, C., Grygorczyk, R. and Ferrier, J., 1989. Osteoblastic cells have L-type calcium channels. *Bone and Mineral*, 7(2), pp.137-148.

Khadra, A., Tomić, M., Yan, Z., Zemkova, H., Sherman, A. and Stojilkovic, S., 2013. Dual Gating Mechanism and Function of P2X7 Receptor Channels. *Biophysical Journal*, 104(12), pp.2612-2621.

Korkotian, E., & Segal, M., 2011. Synaptopodin regulates release of calcium from stores in dendritic spines of cultured hippocampal neurons. *The Journal of Physiology*, 589(24), pp. 5987–5995.

LeBeau, A., Van Goor, F., Stojilkovic, S. and Sherman, A., 2000. Modeling of Membrane Excitability in Gonadotropin-Releasing Hormone-Secreting Hypothalamic Neurons Regulated by Ca2+-Mobilizing and Adenylyl Cyclase-Coupled Receptors. *The Journal of Neuroscience*, 20(24), pp.9290-9297.

Lehnert, J. and Khadra, A., 2019. How Pulsatile Kisspeptin Stimulation and GnRH Autocrine Feedback Can Drive GnRH Secretion: A Modeling Investigation. *Endocrinology*, 160(5), pp.1289-1306.

Li, Y. and Rinzel, J., 1994. Equations for InsP3 Receptor-mediated [Ca2+]i Oscillations Derived from a Detailed Kinetic Model: A Hodgkin-Huxley Like Formalism. *Journal of Theoretical Biology*, 166(4), pp.461-473.

Mackay, L. et al., 2016. Systematic Characterization of Dynamic Parameters of Intracellular Calcium Signals. *Frontiers in Physiology*, 7.

Mikolajewicz, N., Smith, D., Komarova, S. and Khadra, A., 2021. High-affinity P2Y2 and low-affinity P2X7 receptor interaction modulates ATP-mediated calcium signaling in murine osteoblasts.

North, R., 2002. Molecular Physiology of P2X Receptors. *Physiological Reviews*, 82(4), pp.1013-1067.

Peverini, L., Beudez, J., Dunning, K., Chataigneau, T. and Grutter, T., 2018. New Insights Into Permeation of Large Cations Through ATP-Gated P2X Receptors. *Frontiers in Molecular Neuroscience*, 11.

Putney, J., 2010. Pharmacology of Store-operated Calcium Channels. *Molecular Interventions*, 10(4), pp.209-218.

Smith, N. and Crampin, E., 2004. Development of models of active ion transport for whole-cell modelling: cardiac sodium–potassium pump as a case study. *Progress in Biophysics and Molecular Biology*, 85(2-3), pp.387-405.

Wang, S.-Q. et al., 2004. Imaging MICRODOMAIN Ca 2+ in muscle cells. *Circulation Research*, 94(8), pp.1011–1022.

Xing, S., Grol, M., Grutter, P., Dixon, S. and Komarova, S., 2016. Modeling Interactions among Individual P2 Receptors to Explain Complex Response Patterns over a Wide Range of ATP Concentrations. *Frontiers in Physiology*, 7.

Yavropoulou, M. P., & Yovos, J. G. (2016). The molecular basis of bone mechanotransduction. *Journal of musculoskeletal & neuronal interactions*, 16(3), 221–236.

Zeng, S., Li, B., Zeng, S. and Chen, S., 2009. Simulation of Spontaneous Ca2+ Oscillations in Astrocytes Mediated by Voltage-Gated Calcium Channels. *Biophysical Journal*, 97(9), pp.2429-2437.